ACS SENSORS

pubs.acs.org/acssensors

Article

3D Layer-By-Layer Pd-Containing Nanocomposite Platforms for Enhancing the Performance of Hydrogen Sensors

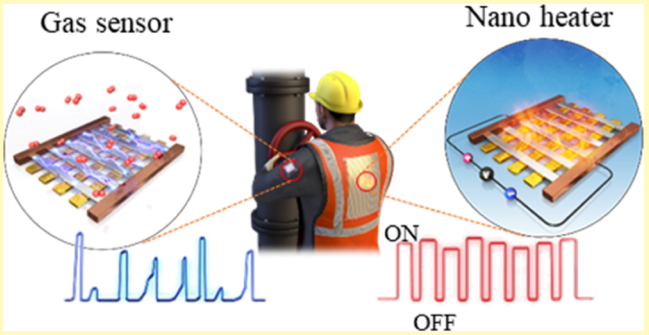
Zhi-Jun Zhao, Jiwoo Ko, Junseong Ahn, Moonjeong Bok, Min Gao, Soon Hyoung Hwang, Hyeok-Joong Kang, Sohee Jeon, Inkyu Park,* and Jun-Ho Jeong*

Cite This: *ACS Sens.* 2020, 5, 2367−2377

Read Online

ACCESS | Metrics & More | Article Recommendations | Supporting Information

ABSTRACT: Herein, a nanowelding technique is adopted to fabricate three-dimensional layer-by-layer Pd-containing nanocomposite structures with special properties. Nanowires fabricated from noble metals (Pd, Pt, Au, and Ag) were used to prepare Pd−Pd nanostructures and Pd−Au, Pd−Pt, Pd−Ag, and Pd−Pt−Au nanocomposite structures by controlling the welding temperature. The recrystallization behavior of the welded composite materials was observed and analyzed. In addition, their excellent mechanical and electrical properties were confirmed by performing 10,000 bending test cycles and measuring the resistances. Finally, flexible and wearable nanoheaters and gas sensors were fabricated using our proposed method. In comparison with conventional techniques, our proposed method can not only easily achieve sensors with a large surface area and flexibility but also improve their performance through the addition of catalyst metals. A gas sensor fabricated using the Pd−Au nanocomposites demonstrated 3.9-fold and 1.1-fold faster H_2 recovery and response, respectively, than a pure Pd−Pd gas sensor device. Moreover, the Pd−Ag nanocomposite exhibited a high sensitivity of 5.5% (better than that of other fabricated gas sensors) for 1.6% H_2 concentration. Therefore, we believe that the fabricated nanocomposites appear promising for wide applications in wearable gas sensors, flexible optical devices, and flexible catalytic devices.



KEYWORDS: *3D layer-by-layer nanostructures, Pd-containing nanocomposites, nanoheater, hydrogen sensing, flexible and wearable device*

In recent years, flexible and wearable devices have emerged in various fields, including optics,[1−3] medicine,[4,5] biosensing,[6−8] and electronics.[9−12] Recently, nanocomposite structures have been widely used to improve the performances of these devices, which has led to higher requirements for nanofabrication to meet the demands of specific applications. In particular, noble metals including silver (Ag), gold (Au), palladium (Pd), and platinum (Pt) have been widely applied in plasmonic devices, metasurfaces, biosensing, and gas sensors. Among these noble metals, Pd is widely used to fabricate hydrogen (H_2) sensors owing to its special reaction with H_2 and can be used to fabricate flexible and wearable devices because of the flexibility of the metal relative to general gas sensors fabricated using brittle metal oxide materials. In addition, Ag, Au, and Pt are used as catalysts in gas sensors, photocatalysis (plasmonic effect), solar cells, and electrochemistry.[13,14] For example, the sensitivity, response speed, and recovery time are very important for gas sensors; Ag, Au, and Pt have thus been used as catalysts in order to improve the performance of gas sensors. Therefore, the fabrication of high-quality nanocomposite structures is required. Many conventional micro-/nano-patterning methods have been developed such as lithography,[15−17] nanotransfer,[18−20] and direct laser wiring.[21−23] These methods have solved some production issues by increasing the patterning resolution and enabling the fabrication of large surface area nanostructures on flexible substrates. However, the fabrication of well-arrayed nanocomposite structures using conventional methods is challenging. Therefore, many researchers have proposed self-assembly and spray-coating and spin-coating methods to fabricate nanocomposite structures for application in catalytic devices,[24−26] soft actuators,[27,28] energy-harvesting devices,[29,30] and solar cells.[31,32] These nanocomposite structures have mostly been fabricated via hydrothermal methods,[33] chemical reduction,[34] room temperature aging,[35] and solvothermal methods.[36] In addition, conventional electrochemical deposition was used to fabricate the Pd−Au−Pt nanocomposite structures.[37] Agglomerated Ag−Pd nanocomposites were fabricated by the addition of sodium borohydride for H_2

Received: January 30, 2020
Accepted: April 23, 2020
Published: April 23, 2020



Downloaded via KOREA ADVANCED INST SCI AND TECHLGY on November 21, 2022 at 13:35:05 (UTC).
See https://pubs.acs.org/sharingguidelines for options on how to legitimately share published articles.

ACS Publications

© 2020 American Chemical Society

https://dx.doi.org/10.1021/acssensors.0c00211
ACS Sens. 2020, 5, 2367−2377

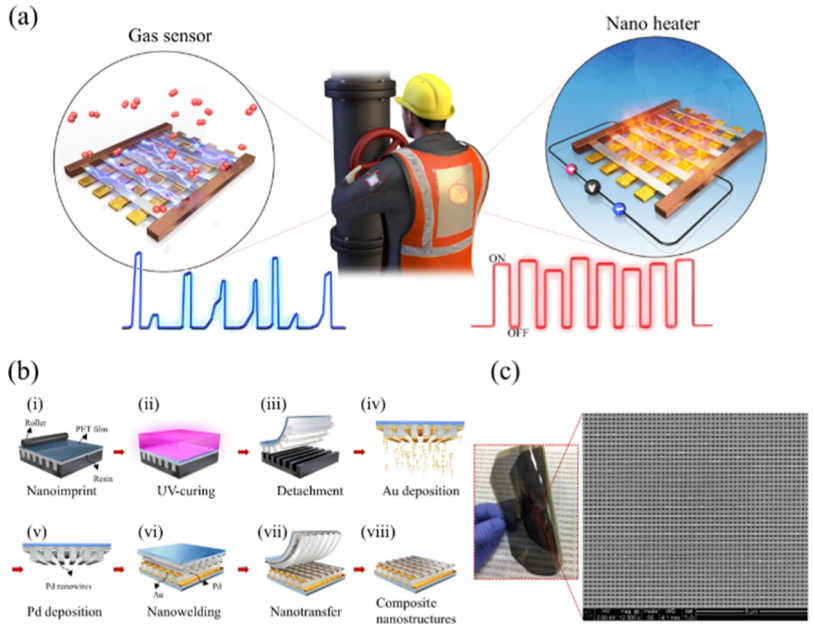


Figure 1. Schematic of the flexible and wearable nanoheater and gas sensor. (a) Conceptual image of a nanoheater and a gas sensor embedded in a cloth. (b) Nanofabrication process: (i) nanoimprinting, (ii) UV-curing, (iii) detachment from the polymer mold, (iv,v) metal deposition for the formation of metal nanostructures, (vi) nanowelding process, (vii) nanotransfer, and (viii) final nanocomposite structures. (c) Photo and SEM image showing the flexibility and the morphology of the nanocomposite structure, respectively.

generation from formic acid at room temperature.[38] The abovementioned nanocomposites were mainly fabricated using metal nanotubes, nanowires (NWs), nanorods, or nanoparticles; this unfortunately limits the shape control of nanocomposite structures. Moreover, large surface area material fabrication is difficult using these methods. In contrast, well-arrayed Ag−TiO_2 nanocomposites have been fabricated by nanoimprint lithography and electron beam evaporation, with demonstrated applications in dye-sensitized solar cells,[39] photocatalysts,[40] and polarization-dependent color filters.[41]

To further improve the nanocomposites, our group proposed a novel method for the fabrication of three-dimensional (3D) grid-like Ag−TiO_2 and Ag−Au nanocomposites for photocatalysis[42] and polarization color filters[43] using nanowelding technique. Until now, we have only studied nanoscale composites comprising low-melting temperature noble metals (Ag and Au). To expand the range of applications of the developed nanomaterials and fabricate well-arrayed nanocomposite structures, in this work, we attempted to fabricate various 3D nanocomposite structures based on NWs of high-melting temperature noble metals such as Pd and Pt using the nanowelding technique. We evaluated how the NW thickness and the welding temperature affected the nanocomposite structure. Noble metals Pd and Pt with special properties are widely applied in the catalysis and gas sensor fields; therefore, the resultant nanostructures were subsequently applied as flexible and wearable heaters and gas sensors.

Pd−Au, Pd−Pt, Pd−Ag, and Pd−Pt−Au nanocomposite structures were fabricated by nanowelding the corresponding NW arrays. In addition, the recrystallization behavior of the fabricated samples was evaluated by high-resolution transmission electron microscopy (HRTEM). Their binding energy and composition were analyzed by X-ray photoelectron spectroscopy (XPS) and energy-dispersive X-ray spectroscopy (EDS), respectively; and their mechanical and electrical properties were evaluated by performing 10,000 bending test cycles and conductivity measurements, respectively. Finally, flexible and wearable nanoheaters and gas sensors were fabricated using the proposed method. In comparison with conventional techniques, our proposed method not only easily achieves sensors with a large surface area and flexibility but also improves their performance through the addition of catalyst metals. A gas sensor fabricated using the Pd−Au nanocomposites demonstrated 3.9-fold and 1.1-fold faster H_2 recovery and response, respectively, than a pure Pd−Pd gas sensor device. Moreover, Pd−Ag nanocomposites exhibited a high sensitivity of 5.5% (better than that of other fabricated gas sensors) for the 1.6% H_2 concentration. We believe that the fabricated 3D composite nanostructures will have significant applications in various fields including catalysis, gas sensing, and electrochemistry.

EXPERIMENTAL SECTION

Fabrication. Flexible and wearable nanoheaters and gas sensors were fabricated from the composite nanostructures. Schematics of the devices are shown in Figure 1a, alongside a conceptual image showing how the devices could be embedded in a cloth. The nanofabrication process is demonstrated in Figure 1b. A nanocomposite sample with a large surface area exhibited good bendability and uniform morphology, as shown in Figure 1c. First, a nanoimprinted resin was chosen to be coated on a Si template with dimensions of 100 nm (width) × 100 nm (space) × 150 nm (depth) to fabricate periodic patterns, then the resin coating on the Si template was covered with polyethylene terephthalate (PET), and rolling was performed on the substrate to enable the resin to thoroughly penetrate the nanopatterns of the Si template (see Figure 1b(i)). UV-curing was performed for 90 s sessions in order to complete the polymerization process (see Figure 1b(ii)). The polymer mold with nanopatterns was then detached from the Si master (see Figure 1b(iii)). Then, noble metals (Pd, Pt, Ag, and Au) were vertically deposited on the polymer mold to obtain the metal nanostructures (see Figure 1b(iv,v)). Two such samples with different kinds of metal nanostructures were aligned to form a

https://dx.doi.org/10.1021/acssensors.0c00211
ACS Sens. 2020, 5, 2367−2377

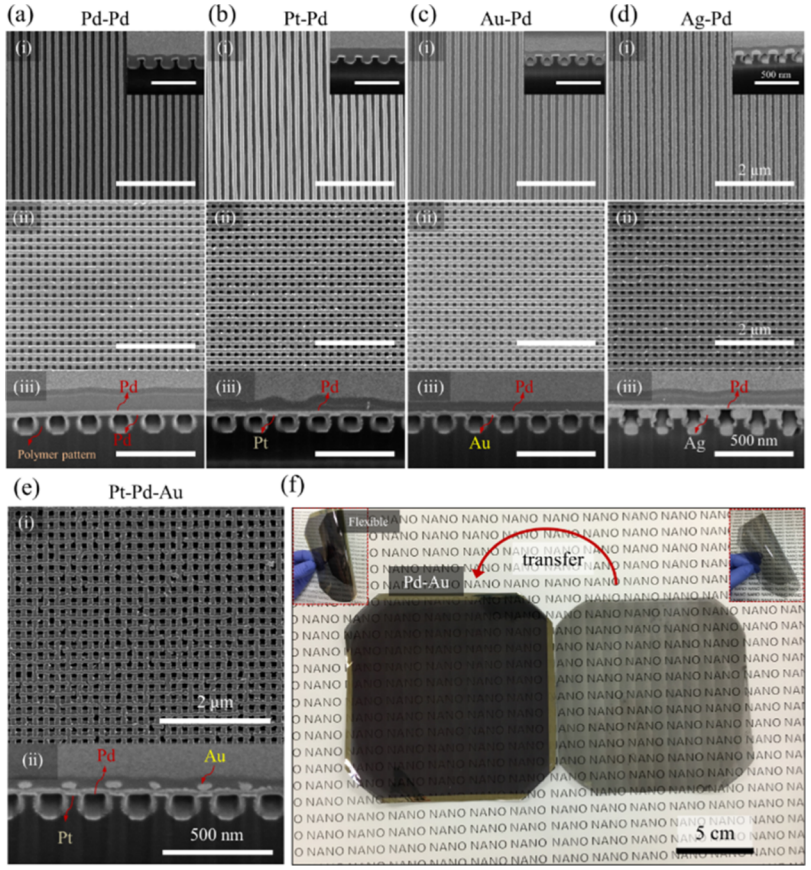


Figure 2. Surface and cross-section morphologies of the fabricated metal NWs and layer-by-layer nanocomposite structures. (a) Pd NWs and Pd−Pd grid-like nanostructures. (b) Pt NWs and Pt−Pd nanocomposite structures. (c) Au NWs and Au−Pd nanocomposite structures. (d) Ag NWs and Ag−Pd nanocomposite structures. (i) Surface morphologies of metal NWs (scale bar: 2 μm). The insets show FIB-SEM cross-sectional images (scale bar: 500 nm). (ii) Surface morphologies of metal−metal grid-like nanostructures and nanocomposite structures (scale bar: 2 μm). (iii) SEM-FIB cross-sectional images (scale bar: 500 nm; metals are indicated using different-colored letters). (e) Surface and cross-section morphologies of Pt−Pd−Au nanocomposite structures. (i) Surface morphology of the nanocomposite structure (scale bar: 2 μm). (ii) Corresponding cross-sectional image (scale bar: 500 nm; metal layer is marked). (f) Photograph of a large-area sample (120 × 120 mm). The inset shows the flexibility of the sample.

crisscross structure, and nanowelding was performed at the temperature and pressure of thermal nanoimprinting (Hutem Co, Korea) (see Figure 1b). It is worth noting that, in this process, the heating temperature is determined by the melting point and the thickness of metals. Wronski and Berman and Curzon predicted the size-dependent melting temperatures of noble metals on a nanoscale.[44,45] In addition, several other researchers have investigated the melting points of metals on a nanoscale as well as the nanowelding technique. Therefore, different heating temperatures were used for different metals. The corresponding nanowelding conditions are provided in the later sections. Finally, 3D nanocomposite structures were obtained after the detachment process (see Figure 1b(vii,viii)).

Based on this fabrication process, Pd, Pt, Au, and Ag metals were deposited onto patterned polymer molds to form metal NW arrays, followed by a nanowelding process to bond the NW arrays at a 90° angle to form Pd−Au, Pd−Pt, Pd−Ag, and Pd−Pt−Au nanocomposite structures. The preparation of the patterned polymer mold and the NW fabrication and nanocomposites are explained below.

The polymer molds were prepared using a nanopatterned Si stamp. A pattern of repeating parallel lines (100 nm width × 200 pitch × 150 nm depth) was prepared on the stamp via a KrF lithography process. To ensure easy separation of the silicon stamp from the polymer mold, the stamp was surface-treated with trichloro(1*H*,1*H*,2*H*,2*H*-perfluorooctyl)silane at 80 °C for 30 min. Two kinds of imprinted ultraviolet (UV)-curable resins with different surface energies were used to make the polymer molds: RM-311 (Minuta Technology Co., Ltd., Korea) and OrmoStamp (MicroResist Technology, Germany). The surface energies can be referenced from a previous work.[46] To prepare the polymer mold, the imprint resin was coated on the surface of the Si stamp and a PET film with a thickness of 120 μm was used to cover the resin. Pressure was applied to allow the resin to fill the nanopatterns in the Si stamp, and UV curing was performed for 90 s to polymerize the resin. Then, the PET film was lifted from the Si stamp, along with the patterned polymer. Subsequently, UV curing was performed to fully polymerize the patterned polymer.

Different kinds of noble metal NW arrays (Pd, Pt, Au, and Ag; 100 nm width × 200 nm pitch × 20 nm thickness) were fabricated by depositing the corresponding metals onto the patterned polymer on the PET film by electron beam evaporation (Daeki Hi-Tech Co., Ltd., Korea) at a rate of 1 Å s^{-1}. Subsequently, nanowelding of the metal NW arrays was implemented using an abovementioned method[47] at a pressure of 5 bar and a temperature of over 160 °C for 10 min by thermal nanoimprinting (Hutem Co, Korea).

Application. The temperature of the nanoheaters could be changed by adjusting the DC voltage across the nanostructure via a power supply (UP-3005D, UNICORN TMI, Korea). To evaluate the heating behavior, a data logger (midi LOGGER GL220, Graphtec, Japan) was used to record the temperature of the nanoheaters, and infrared (IR) thermal imaging was performed using an IR thermal camera (E6, FLIR Systems, USA).

The gas sensing performance of the fabricated nanostructures was evaluated in a sealed chamber with a probe station. H_2 gas with a certain concentration was injected into the sealed chamber, and the real-time current was recorded using a sourcemeter (Keithley 2635B).

https://dx.doi.org/10.1021/acssensors.0c00211
ACS Sens. 2020, 5, 2367−2377

N_2 and O_2 gases were mixed at a 4:1 ratio to represent the basic air environment. The concentrations of the gases were controlled using a mass flow controller.

Characterization. The morphologies and cross-sections of the fabricated samples were, respectively, observed by field-emission SEM (FESEM; Sirion, FEI, The Netherlands) and focused ion beam scanning electron microscopy (FIB-SEM) (Helios Nanolab, FEI, The Netherlands). HRTEM (JEM-ARM200FM, JEOL, Japan) was performed to confirm the recrystallization of the two different metals. XPS (K-Alpha+, Thermo Fisher Scientific, Inc.) was performed to analyze the binding energy of the interfaces of different metals. An etching method was used to analyze the depth profile using a monoatomic Ar ion gun (energy: 500 eV; raster size: 1 × 1 mm; angle: 30°). The etching process was implemented at intervals of 20 s for 80 cycles. To prevent the charging of samples, a flood gun with a pass energy of 151.8 eV was used for neutralization. An X-ray beam of 200 μm and an Al Kα source were used to analyze and measure the fabricated samples. In addition, X-ray diffraction (XRD; SmartLab, MXD10, Rigaku Corporation) was used to analyze the crystallinities and orientations of the nanocomposite structures.

RESULTS AND DISCUSSION

Morphologies and Cross-Sectional Images of Pd-Containing Nanocomposites. Bulk metals have an inherently high melting temperature, often exceeding 1000 °C. However, noble metals reportedly have lower melting temperatures on a nanoscale.[48] Considering this, we fabricated various nanocomposite structures from noble metal NW arrays using nanowelding technique. Figure 2a(i),b(i),c(i),d(i) show the morphological SEM images of Pd, Pt, Au, and Ag NWs, respectively; FIB-SEM cross-sectional images of the NWs are shown in the insets. Pd−Pd, Pt−Pd, Au−Pd, and Ag−Pd nanocomposite structures were fabricated by nanowelding the corresponding NW arrays at a 90° angle; their morphologies are shown in Figure 2a(ii),b(ii),c(ii),d(ii), respectively, and the corresponding cross-sectional images are shown in Figure 2a(iii),b(iii),c(iii),d(iii), respectively. Figure 2a−d show that the nanocomposite structures did not have any defects.

The melting temperatures of bulk Pd, Pt, Au, and Ag are 1555, 1768.3, 1064, and 961.8 °C, respectively. In previous works,[48,49] we describe how the melting temperatures of nanoscale Au and Ag samples depend on the thickness of the metals. We found that the sequence of melting temperatures on a nanoscale could be judged by the melting temperature of bulk metals of the same size. Therefore, the welding temperature of Pd and Pt on a nanoscale can probably be estimated based on previous results. Welding at temperatures of 130−150 °C resulted in incomplete nanowelding of the Pd−Pd nanostructures, as shown in the SEM images in Figure S1. From these images, the appropriate welding temperature of the Pd NWs was estimated as 160 °C. Interestingly, 90 nm-thick Ag NWs were observed in the Ag−Pd nanocomposite (Figure 2d). This is because thin Ag NWs have a lower melting point that cannot overcome the welding temperature of Pd.

To investigate the effect of NW thickness, which can affect its melting point on a nanoscale, Ag NWs with a thickness of 40 nm were nanowelded with Pd NWs at 160 °C; the SEM images are shown in Figure S2. To show the diversity of the nanocomposite structures, three kinds of metal nanocomposites based on Pt, Pd, and Au were fabricated by the nanowelding method. Importantly, Pt−Pd nanocomposite structures were fabricated by nanowelding at 190 °C because of the higher melting point of Pt, while Pd−Au was fabricated at 160 °C. Figure 2e shows the surface and cross-section morphologies of a Pd−Pt−Au nanocomposite structure. It is well known that conventional methods are not suitable for the fabrication of large surface area nanostructures on most types of substrates. However, as demonstrated in Figure 2f, the fabrication of flexible and large surface area samples (120 × 120 mm) was possible by this technique.

HRTEM and EDS Mapping of Pd-Containing Nanocomposites. To better observe the recrystallization and the position of the fabricated samples, HRTEM and EDS mapping were performed, as shown in Figure 3. To clearly observe the welding phenomenon, different magnification images of nanostructures are shown in Figure 3(i−iv). The top and bottom insets in Figure 3(iv) show the crystallized structures and the fast Fourier transform (FFT) images, respectively. The compositions of the nanostructures were confirmed by EDS mapping, as shown in Figure 3(v−viii). Figure 3 reveals that

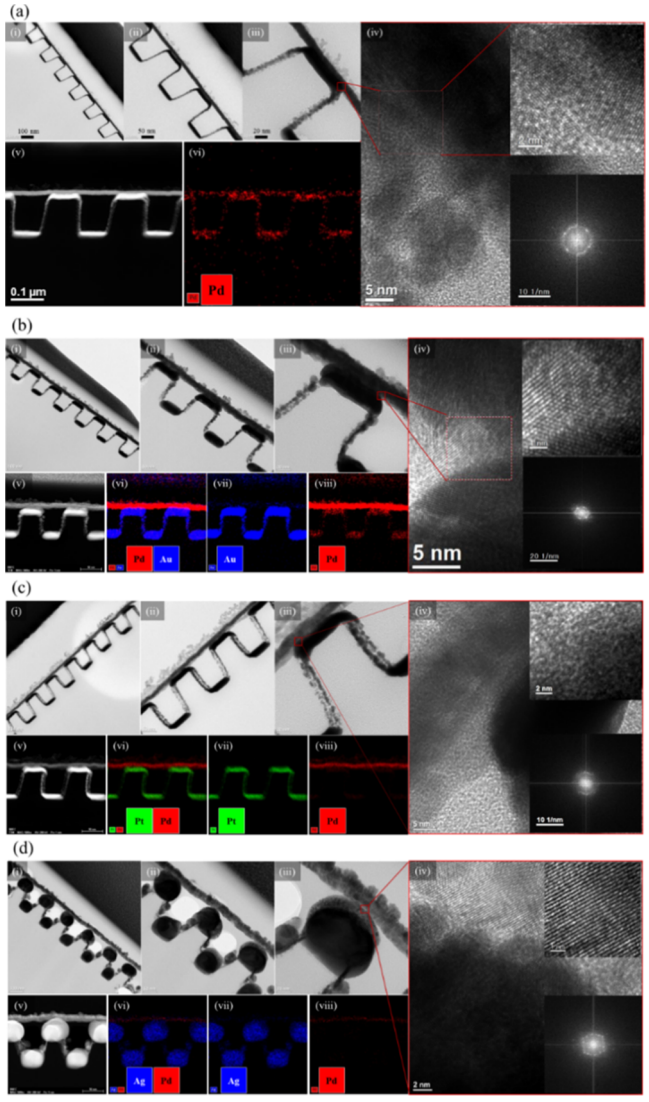


Figure 3. Cross-sectional HRTEM images of the fabricated samples. (a) Pd−Pd nanostructures, (b) Au−Pd nanocomposite structures, (c) Pt−Pd nanocomposite structures, and (d) Ag−Pd nanocomposite structures. (i−iii) Cross-sectional images at different magnifications (scale bars: (i) 100, (ii) 50, and (iii) 20 nm). (iv) High-magnification cross-sectional images (scale: 5 nm). The top and bottom insets show the atomic structures and FFT images, respectively. (v,vi) of (a) and (v−viii) of (b−d) EDS maps of (a) Pd−Pd, (b) Au−Pd, (c) Pt−Pd, and (d) Ag−Pd nanostructures.

https://dx.doi.org/10.1021/acssensors.0c00211
ACS Sens. 2020, 5, 2367−2377

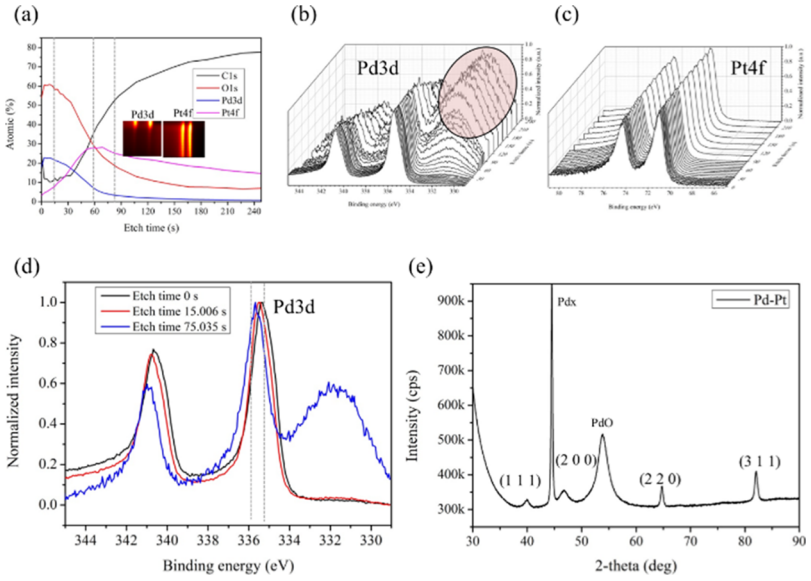


Figure 4. XPS and XRD results of Pd−Pt nanocomposite structures. (a) Variation in the relative percentages of different elements of Pd−Pt nanostructures with etching time. (b) Pd 3d and (c) Pt 4f binding energies of Pd and Pt NWs in the nanocomposite structures etched for different periods. (d) Pd 3d binding energy at a critical etching time. XRD spectrum of Pd−Pt nanocomposite structures. (e) XRD result of Pd−Pt nanocomposite structures.

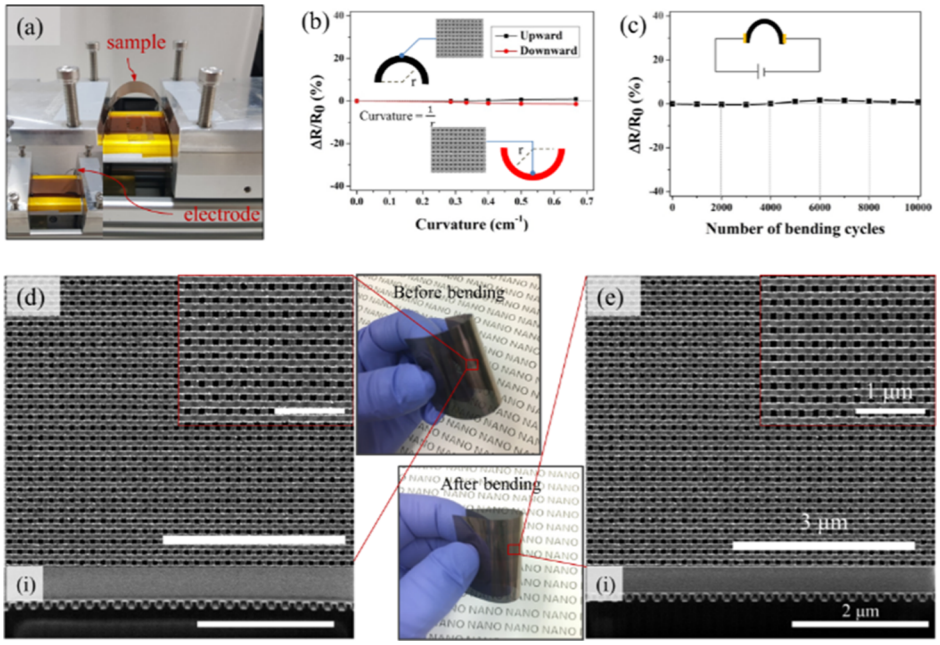


Figure 5. Mechanical and electrical properties of the Pd−Au nanocomposite before and after cyclic bending tests. (a) Photograph of the bending tester connected with the fabricated sample using an electrode. (b,c) Rate of change in the resistance ($\Delta R/R_0$) with upward and downward bending of the flexible film comprising the fabricated nanostructures depending on the change in the curvature ($1/r$) and the number of bending cycles. (d,e) Surface and cross-sectional images before and after the bending test (scale bar: 3 μm; scale bar of inset: 1 μm; and scale bar of cross-sectional images (i) 2 μm).

the nanocomposite structures were easily fabricated by the proposed method. In addition, the HRTEM and EDS mapping images of the Pd−Pt−Au nanocomposite structures (Figure S3) confirm the diversity of the proposed nanofabrication method.

XPS and XRD Analyses. To evaluate the binding energy, chemical composition, and crystallization orientation of the fabricated nanostructures, XPS and XRD were performed. Figure 4 shows the XPS and XRD spectra of the Pd−Pt nanocomposite structures. XPS etching was implemented to observe the binding energy of the interface of Pd and Pt NWs. The depth profile analysis of the fabricated sample is shown in Figure 4a. The relative percentage of each element was dependent on the change in the etching time. At an etching time of about 15 s, the relative percentage of Pd 3d began to decrease, while that of Pt 4f started to increase. After about 75 s of etching, the percentage of Pd 3d was close to 0. Based on this, we can conclude that the etching reached the interface between Pd and Pt at around 60−75 s. The binding energies of Pd 3d and Pt 4f with different etching times are displayed in

https://dx.doi.org/10.1021/acssensors.0c00211
ACS Sens. 2020, 5, 2367−2377

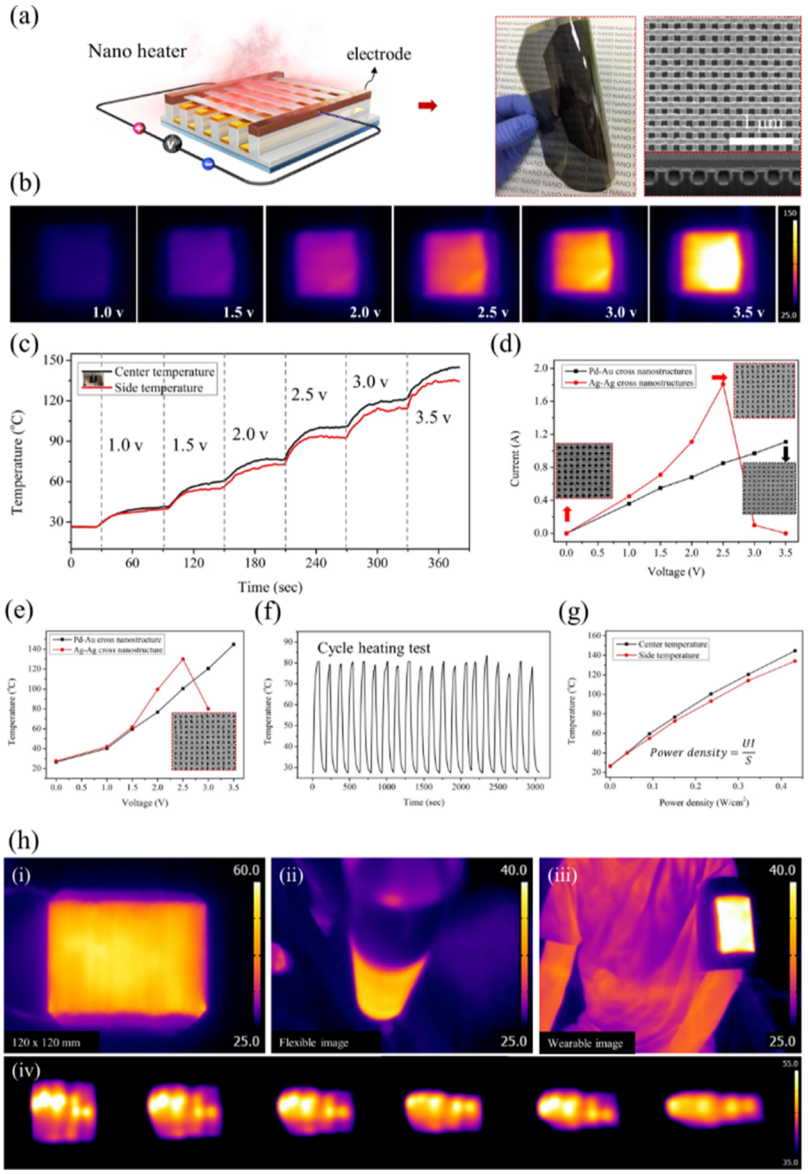


Figure 6. Characterization of Pd−Au nanocomposite structure-based nanoheaters. (a) Schematic of a nanoheater with a photograph showing the flexibility of the nanoheater, and morphology (top and cross-sectional images) of nanoheater. (b) IR images of the nanoheater under different applied voltages from 1 to 3.5 V at intervals of 0.5 V (sample area: 30 mm × 30 mm). (c) Time-dependent changes in the average temperatures in the center and on side of the nanoheater. (d,e) Comparison of two kinds of nanoheaters based on Pd−Au and Ag−Ag cross nanostructures under different applied voltages. (f) Cyclic heating test curves of the nanoheater. (g) Change in the temperature of the nanoheater with input power density. (h) (i−iii) IR images of the large surface area, flexible, and wearable nanoheater and (iv) thermal stability test after bending with different curvatures.

Figure 4b,c, respectively. Figure 4b shows that the Pd 3d peak slightly shifted at a critical etching point. The binding energies of the critical etching points are displayed in Figure 4d. A new peak appears at an etching time of 75 s. For reference, the XPS results of Pd−Pd, Pd−Ag, and Pd−Au nanostructures are shown in Figures S4, S5, and S7, respectively, with detailed explanations provided in the captions. The crystal orientation of the Pd−Pt nanocomposite structure was measured by XRD, as shown in Figure 4e. The peaks corresponding to the (111), (200), (220), and (311) crystal directions appeared at 40, 47, 65, and 82°, respectively. By analyzing and comparing with ref 50, we inferred that the two peaks at 44 and 54° represent Pd*x* and PdO, respectively. The XRD spectra of the Pd−Ag and Pd−Au nanocomposite structures are shown in Figures S6 and S8, respectively.

Evaluation of Mechanical and Electrical Properties of Pd-Containing Nanocomposites. To evaluate the mechanical and electrical properties of the fabricated nanostructures, the Pd−Au nanocomposite was selected for bending and resistance tests. Figure 5 shows the mechanical and electrical properties of the flexible Pd−Au nanocomposite film before and after cyclic bending. To perform the bending test and measure the resistance simultaneously, an electrode was connected to the bending tester, as shown in Figure 5a. The rate of change in the resistance [$\Delta R/R_0$, where ΔR is the difference between the resistance after bending and the initial resistance (R_0)] was evaluated during upward and downward bending depending on the change in the curvature ($1/r$, where r is the radius of curvature of the bent film) and the number of bending cycles; the results are shown in Figure 5b,c,

https://dx.doi.org/10.1021/acssensors.0c00211
ACS Sens. 2020, 5, 2367−2377

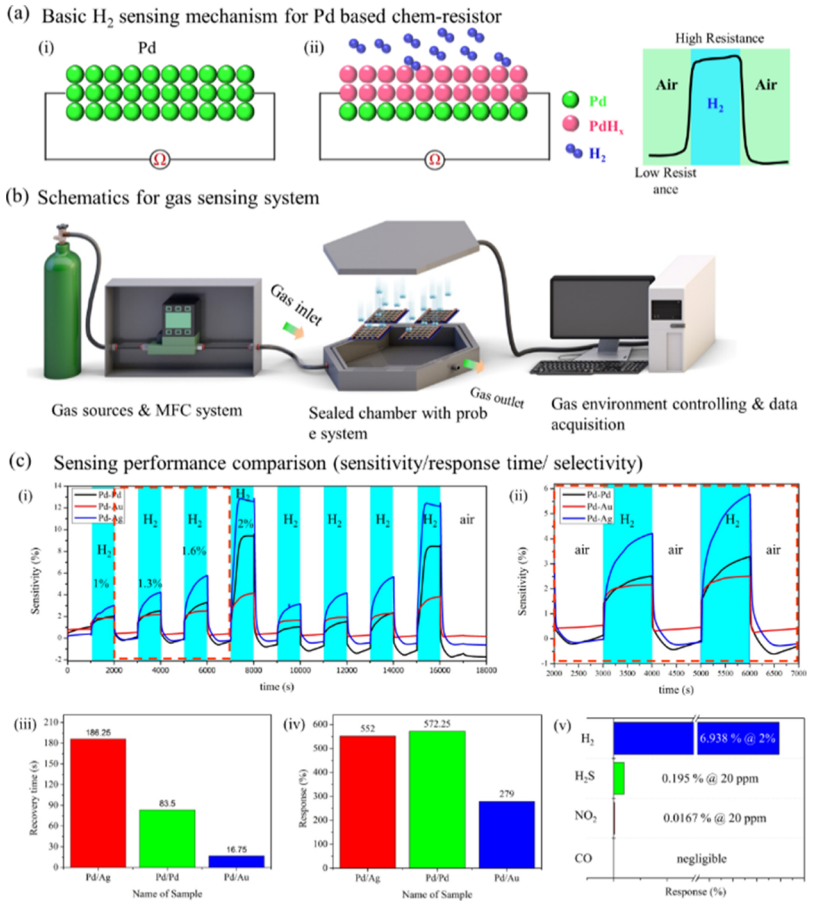


Figure 7. Evaluation of H_2 gas sensors based on the fabricated nanocomposite structures. (a) Basic H_2 sensing mechanism for the Pd-based chemiresistor. (b) Schematic of the gas sensing system. (c) Sensing performance comparison based on the sensitivity, recovery time, response time, and selectivity: (i,ii) Sensitivity of gas sensors based on Pd−Pd, Pd−Ag, and Pd−Au nanostructures, respectively; (iii,iv) comparisons of recovery and response time of the three kinds of gas sensors; and (v) selectivity of the gas sensor toward H_2, H_2S, NO_2, and CO gases.

respectively. The upward and downward samples represent the direction of the nanostructured surface. The bending test was performed for 10,000 bending cycles and the rate of change in the resistance was measured at intervals of 1000 cycles. From Figure 5b,c, we can obtain the $\Delta R/R_0$ values. In addition, the surface and cross-sectional morphologies before and after 10,000 bending cycles were observed by SEM-FIB. As can be seen, the surface nanostructures of the sample were intact even after the cyclic bending test. Thus, we can conclude that our fabricated nanostructures have good mechanical and electrical properties.

Flexible Nanoheaters Based on Pd-Containing Nanocomposites. To evaluate the application of the fabricated samples, they were used to produce nanoheaters. Recently, nanoheaters have become increasingly important for various applications under extremely cold conditions, such as defogging windows and mirrors in cars and for heating solar panels and clothing.[51−55] Thus far, most nanoheaters have been based on silver NWs, copper NWs, and carbon nanotubes, and were prepared by electrospinning, spray-coating, and spin-coating methods.[56−59] Recently, Cui et. Al[60] reported the high-resolution, large-scale printing of highly conductive Ag NWs for flexible and stretchable heaters based on the electrohydrodynamic printing method. However, these methods have limitations in terms of fabricating well-arrayed structures and nanoscale spaces, which means that the existing nanoheaters lack the required uniformity. To overcome these issues, in this study, we fabricated nanoheaters with well-arrayed nanostructures based on noble metal NWs using the nanowelding technique. Figure 6 shows the characterization results of a nanoheater based on the Pd−Au grid-like nanocomposite structure on a PET film. Figure 6a(i−iii) show the schematic image, photograph, and morphology of the fabricated heater, respectively, and Figure 6b shows IR images of the temperature distributions of the film at different DC voltages. The temperature of the heater could be controlled between 25 and 150 °C by adjusting the voltage from 1 to 3.5 V at intervals of 0.5 V. Figure 6c displays the time-dependent change in the average temperature of the nanoheater. To confirm the uniformity of the temperature distributions, the temperatures at the center and on the side of the heater were measured using a temperature sensor; the temperatures at these locations are indicated by the black and red curves, respectively. When the input DC voltage was increased from 0 to 3.5 V at intervals of 0.5 V for every 60 s, the average temperature increased to about 135.5 °C. When the input DC voltage was decreased from 3.5 to 0 V at intervals of 0.5 V every 60 s (Figure S9). At a constant applied voltage, the saturation time of temperature of the heater was checked, and the graph is shown in Figure S10.

The heating performance of the Pd−Au heater was compared with that of an Ag−Ag grid-like nanostructure prepared by the nanowelding method. The morphologies of the Pd−Au and Ag−Ag nanostructures are shown in Figure

https://dx.doi.org/10.1021/acssensors.0c00211
ACS Sens. 2020, 5, 2367−2377

S11. Figure 6d shows how the current of the Pd−Au and Ag−Ag nanostructures changed with variation in the DC voltage, with SEM images of the nanostructures before and after application of the voltage shown in the insets. When a voltage of 2.5 V was applied to the heaters, the current of the Ag−Ag nanostructure instantly dropped to 0, and the heating process was hindered due to the fracture of Ag NWs. In contrast, the Pd−Au nanostructures did not undergo deformation owing to the high melting temperature. The voltage-dependent changes in the temperatures of the two kinds of heaters are shown in Figure 6e. In addition, the time-dependent change in the average temperature of the Ag−Ag nanostructure is shown in Figure S12.

In order to demonstrate the stability of the fabricated nanoheater, a cyclic heating test was performed by repeatedly applying a DC voltage to the Pd−Au nanoheater. Figure 6f shows the reliability of this heater, irrespective of the repetition of its on/off functions. The temperature increased linearly with the input power density, as shown in Figure 6g. To demonstrate the large surface area and flexible and wearable properties, a heater with a size of 120 × 120 mm was fabricated based on the Pd and Au NWs by the nanowelding method. Figure 6h shows the IR images of the heater. The flexible and wearable functions are demonstrated in Figure 6h(ii),(iii). The related IR images are provided in Figure S13 for reference. Moreover, bending tests were performed with different curvatures at a constant temperature, and the results are shown in Figure 6h(iv). Bending did not affect the temperature distribution of the heater; therefore, we believe that our fabricated array heater will be important for flexible and wearable electronics.

Flexible Gas Sensors Based on Pd-Containing Nanocomposites. To further demonstrate the practicality of the nanocomposite structures, a H_2 gas sensor was fabricated and evaluated. H_2 is widely considered an important material for promising next-generation green energy resources.[61,62] However, it is an explosive gas with a lower flammability limit of 4% in air.[63] Moreover, because H_2 is colorless and odorless, it is difficult to detect with human senses. Thus, the development of H_2 gas sensors with improved sensitivity, response, selectivity, and stability is necessary. Until now, Pd is mainly used as a functional material for detecting H_2 because it can easily absorb the H_2 gas and convert it into palladium hydride (PdH_X) at room temperature, thereby changing the electrical and optical properties of the material.[64,65]

Recently, Pt, Au, and Ag metals have been used to fabricate nanocomposite structures to enhance the performance of gas sensors. For example, Wang and Feng[66] demonstrated that a Pd−Ag film with a high H_2 permeability realized a 60-fold faster H_2 sensing speed than a pure Pd film. Jang et al.[67] reported on the development of hollow Pd−Ag alloy NWs (Pd@Ag HNWs) using the electrodeposition of lithographically patterned silver NWs for enhancing the performance of an H_2 sensor. Li et al.[68] prepared Pd@Pt NWs for accelerated H_2 gas detection, and Namba et al.[69] investigated the acceleration of H_2 absorption at Pd−Au surface alloys by means of thermal desorption spectroscopy and hydrogen depth profiling with nuclear reaction analysis. In addition, Moreno et al.[70] reported on the sensing characteristics of an optical hydrogen sensor based on a Pd/Au thin film, which showed a sensitivity of ∼0.24% with a response time of 23 s for 2% H_2. Therefore, it can be concluded that Pd-containing nanocomposite structures are important for gas sensing applications. However, in previous researches, the flexibility and wearability of the substrates and the arrangement of uniform nanocomposite structures in a large scale were limited. In this work, various well-arrayed nanocomposite structures fabricated on flexible substrates were employed and evaluated as H_2 gas sensors toward flexible and wearable applications.

The basic H_2 sensing mechanism for a Pd-based chemiresistor is shown in Figure 7a. When H_2 gas was injected into a sealed chamber containing the fabricated gas sensor, H_2 was absorbed by the Pd material and converted into PdH_X, increasing the resistance. The schematic of the gas sensing system is shown in Figure 7b. The sensing performances of the gas sensors based on Pd−Ag, Pd−Au, and Pd−Pd nanostructures were compared in terms of sensitivity, response and recovery time, and selectivity. The sensitivities of the Pd−Pd, Pd−Ag, and Pd−Au gas sensors toward 1−2% H_2 gas are shown in Figure 7c(i,ii), respectively. The recovery and response times of the three kinds of gas sensors are, respectively, shown in Figure 7c(iii,iv). Notably, the recovery and response time of the Pd−Au gas sensor was the shortest. This is because Au can accelerate H_2 absorption, leading to the rapid formation of PdH_X and thereby increase the resistance. This is consistent with a previous report.[68] The recovery and response times of the Pd−Ag gas sensor were longer than those of the Pd−Pd gas sensor; however, the Pd−Ag nanocomposite structure exhibited remarkable sensitivity because Ag can enhance H_2 gas detection.[66]

Applied voltage-controlled H_2 sensing was implemented to demonstrate the sensing effect of the fabricated nanocomposite structures as the reference. The results are provided in Figure S14. To determine the selectivity of the sensor toward H_2 gas, selectivity tests were performed using H_2S, NO_2, and CO gases, and the results are shown in Figure 7c(v). The detailed experimental results are presented in Figure S15. The results confirm excellent H_2 selectivity of the gas sensor. By researching various gas sensors based on different nanocomposite structures, we can better confirm the importance of our fabricated nanocomposite structures in improving the performances of various devices including gas sensors, catalysts, and energy harvesting materials. Finally, in order to demonstrate the limit of detection, the added experiment was implemented (Figure S16). The results of our experiments revealed that the gas sensor starts to operate from an H_2 concentration of 0.5%, and an H_2 concentration of 2% can be detected. This, however, allows us to detect the gas at up to the explosive limit (4%). We will focus on designing further nanocomposite structures using our proposed method to enhance the performance of gas sensors in future research.

CONCLUSIONS

In summary, 3D layer-by-layer Pd-containing nanocomposite structures based on Pt, Au, and Ag NWs were successfully fabricated on flexible and wearable substrates using the nanowelding technique. Pd−Pd grid-like nanostructures and Pd−Pt, Pd−Au, Pd−Ag, and Pd−Pt−Au nanocomposite structures were fabricated without any defects using our proposed method. The results showed that the large surface area, flexible, and wearable heater comprising the well-arrayed nanostructures exhibited better performance compared with conventional heaters based on random Ag NWs. Moreover, as compared to conventional gas sensors fabricated using brittle metal oxide materials, Pd-containing gas sensors can be easily fabricated on a flexible and wearable substrate while realizing a

https://dx.doi.org/10.1021/acssensors.0c00211
ACS Sens. 2020, 5, 2367−2377

good performance. Additionally, the experiments demonstrated that the addition of Ag and Au metals could make a significant contribution to improving the response time, recovery time, and sensitivity of the gas sensor. We believe that our fabrication method can be applied in various fields such as electrocatalysts, gas sensors, and optics.

■ ASSOCIATED CONTENT

Supporting Information

The Supporting Information is available free of charge at https://pubs.acs.org/doi/10.1021/acssensors.0c00211.

SEM morphologies of the fabricated nanostructures at different welding temperatures, SEM morphologies of the nanocomposite structures fabricated using ultrathin metal NWs, cross-sectional HRTEM images and EDS mapping images of Pt−Au−Pd nanocomposite structures, binding energies of the elements and peak positions of Pd 3d, binding energies of the elements and peak positions of Pd 3d and Ag 3d for Pd−Ag nanocomposite structures, XRD spectra of Pd−Ag nanocomposite structures, binding energies of the elements and peak positions of Pd 3d and Au 4f for Pd−Au nanocomposite structures, XRD spectra of Pd−Ag nanocomposite structures, temperature change of the Pd−Au heater, saturation of temperature of the heater at a constant voltage, comparison of Pd−Au and Ag−Ag heaters after heating at an applied voltage, temperature change of the Ag−Ag heater with an applied voltage, IR images of the Pd−Au nanoheater, and evaluation of the H_2 gas sensor depending on different applied voltages, selectivity of the gas sensor toward NO_2, H_2S, and CO gases, and evaluation of the fabricated Pd−Au gas sensor at a H_2 concentration of 0.5−2% (PDF)

■ AUTHOR INFORMATION

Corresponding Authors

Inkyu Park − *Department of Mechanical Engineering, Korea Advanced Institute of Science and Technology, Deajeon 34141, Republic of Korea;* orcid.org/0000-0001-5761-7739; Phone: +82-423503240; Email: inkyu@kaist.ac.kr

Jun-Ho Jeong − *Nano-Convergence Mechanical System Research Center, Korea Institute of Machinery and Materials, Daejeon 34113, South Korea; Department of Nano Mechatronics, University of Science and Technology, Daejeon 34113, South Korea;* orcid.org/0000-0003-0671-0225; Phone: +82-4286-876-04; Email: jhjeong@kimm.re.kr

Authors

Zhi-Jun Zhao − *Nano-Convergence Mechanical System Research Center, Korea Institute of Machinery and Materials, Daejeon 34113, South Korea*

Jiwoo Ko − *Nano-Convergence Mechanical System Research Center, Korea Institute of Machinery and Materials, Daejeon 34113, South Korea; Department of Mechanical Engineering, Korea Advanced Institute of Science and Technology, Deajeon 34141, Republic of Korea*

Junseong Ahn − *Nano-Convergence Mechanical System Research Center, Korea Institute of Machinery and Materials, Daejeon 34113, South Korea; Department of Mechanical Engineering, Korea Advanced Institute of Science and Technology, Deajeon 34141, Republic of Korea*

Moonjeong Bok − *Nano-Convergence Mechanical System Research Center, Korea Institute of Machinery and Materials, Daejeon 34113, South Korea*

Min Gao − *Department of Mechanical Engineering, Korea Advanced Institute of Science and Technology, Deajeon 34141, Republic of Korea*

Soon Hyoung Hwang − *Nano-Convergence Mechanical System Research Center, Korea Institute of Machinery and Materials, Daejeon 34113, South Korea*

Hyeok-Joong Kang − *Nano-Convergence Mechanical System Research Center, Korea Institute of Machinery and Materials, Daejeon 34113, South Korea*

Sohee Jeon − *Nano-Convergence Mechanical System Research Center, Korea Institute of Machinery and Materials, Daejeon 34113, South Korea*

Complete contact information is available at: https://pubs.acs.org/10.1021/acssensors.0c00211

Author Contributions

The manuscript was written through contributions of all authors. Z.-J.Z. performed all experiments, analyzed the data, and wrote the paper. Z.-J.Z., J.K., J.A., M.B., and M.G. discussed the results of nanoheaters and gas sensors. Z.-J.Z., S.H.H., H.-J.K., and S.J. discussed the fabrication of nanocomposite structures. J.-H.J. and I.P. assumed the overall direction of the project. All authors have given approval to the final version of the manuscript.

Notes

The authors declare no competing financial interest.

■ ACKNOWLEDGMENTS

This work was supported by the Center for Advanced Meta-Materials (CAMM), which is funded by the Ministry of Science, ICT and Future Planning, Korea, through the Global Frontier Project (CAMM-No. 2014M3A6B3063707).

■ REFERENCES

(1) Fernandes, M. S.; Lee, K. S.; Ram, R. J.; Correia, J. H.; Mendes, P. M. Flexible PDMS-based dry electrodes for electro-optic acquisition of ECG signals in wearable devices. *Conf. Proc. IEEE Eng. Med. Biol. Sci.* **2010**, *2010*, 3503−3506.

(2) Mecerreyes, D.; Marcilla, R.; Ochoteco, E.; Grande, H.; Pomposo, J. A.; Vergaz, R.; Sánchez Pena, J. M. A simplified all-polymer flexible electrochromic device. *Electrochim. Acta* **2004**, *49*, 3555−3559.

(3) Leydecker, T.; Herder, M.; Pavlica, E.; Bratina, G.; Hecht, S.; Orgiu, E.; Samorì, P. Flexible non-volatile optical memory thin-film transistor device with over 256 distinct levels based on an organic bicomponent blend. *Nat. Nanotechnol.* **2016**, *11*, 769−775.

(4) Khan, Y.; Ostfeld, A. E.; Lochner, C. M.; Pierre, A.; Arias, A. C. Monitoring of vital signs with flexible and wearable medical devices. *Adv. Mater.* **2016**, *28*, 4373−4395.

(5) Singh, N.; Singh, A. K.; Singh, V. K. Design and performance of wearable ultrawide band textile antenna for medical applications. *Microw. Opt. Technol. Lett.* **2015**, *57*, 1553−1557.

(6) Imani, S.; Bandodkar, A. J.; Vinu Mohan, A. M.; Kumar, R.; Yu, S.; Wang, J.; Mercier, P. P. A wearable chemical−electrophysiological hybrid biosensing system for real-time health and fitness monitoring. *Nat. Commun.* **2016**, *7*, 11650.

(7) Han, W.; He, H.; Zhang, L.; Dong, C.; Zeng, H.; Dai, Y.; Xing, L.; Zhang, Y.; Xue, X. A self-powered wearable noninvasive electronic-skin for perspiration analysis based on piezo-biosensing unit matrix of enzyme/ZnO nanoarrays. *ACS Appl. Mater. Interfaces* **2017**, *9*, 29526−29537.

(8) Economou, A.; Kokkinos, C.; Prodromidis, M. Flexible plastic, paper and textile lab-on-a chip platforms for electrochemical biosensing. *Lab Chip* **2018**, *18*, 1812−1830.
(9) Wang, D.; Zhang, Y.; Lu, X.; Ma, Z.; Xie, C.; Zheng, Z. Chemical formation of soft metal electrodes for flexible and wearable electronics. *Chem. Soc. Rev.* **2018**, *47*, 4611−4641.
(10) Yang, Y.; Gao, W. Wearable and flexible electronics for continuous molecular monitoring. *Chem. Soc. Rev.* **2019**, *48*, 1465−1491.
(11) Wu, Z.; Wang, Y.; Liu, X.; Lv, C.; Li, Y.; Wei, D.; Liu, Z. Carbon-nanomaterial-based flexible batteries for wearable electronics. *Adv. Mater.* **2019**, *31*, 1800716.
(12) Liu, Y.; Pharr, M.; Salvatore, G. A. Lab-on-skin: a review of flexible and stretchable electronics for wearable health monitoring. *ACS Nano* **2017**, *11*, 9614−9635.
(13) Guo, S.; Yu, P.; Li, W.; Yi, Y.; Wu, F.; Mao, L. Electron Hopping by Interfacing Semiconducting Graphdiyne Nanosheets and Redox Molecules for Selective Electrocatalysis. *J. Am. Chem. Soc.* **2020**, *142*, 2074.
(14) Feng, T.; Ji, W.; Tang, Q.; Wei, H.; Zhang, S.; Mao, J.; Zhang, Y.; Mao, L.; Zhang, M. Low-Fouling Nanoporous Conductive Polymer-Coated Microelectrode for In Vivo Monitoring of Dopamine in the Rat Brain. *Anal. Chem.* **2019**, *91*, 10786−10791.
(15) Sun, S.; Chong, K. S. L.; Leggett, G. J. Nanoscale molecular patterns fabricated by using scanning near-field optical lithography. *J. Am. Chem. Soc.* **2002**, *124*, 2414−2415.
(16) Altissimo, M. E-beam lithography for micro-/nanofabrication. *Biomicrofluidics* **2010**, *4*, 026503.
(17) Chou, S. Y.; Krauss, P. R.; Renstrom, P. J. Nanoimprint lithography. *J. Vac. Sci. Technol., B: Microelectron. Nanometer Struct.–Process., Meas., Phenom.* **1996**, *14*, 4129−4133.
(18) Zaumseil, J.; Meitl, M. A.; Hsu, J. W. P.; Acharya, B. R.; Baldwin, K. W.; Loo, Y.-L.; Rogers, J. A. Three-dimensional and multilayer nanostructures formed by nanotransfer printing. *Nano Lett.* **2003**, *3*, 1223−1227.
(19) Chanda, D.; Shigeta, K.; Gupta, S.; Cain, T.; Carlson, A.; Mihi, A.; Baca, A. J.; Bogart, G. R.; Braun, P.; Rogers, J. A. Large-area flexible 3D optical negative index metamaterial formed by nanotransfer printing. *Nat. Nanotechnol.* **2011**, *6*, 402−407.
(20) Tran, H.; Bergman, H. M.; Parenti, K. R.; van der Zande, A. M.; Dean, C. R.; Campos, L. M. Hierarchical patterns with sub-20 nm pattern fidelity via block copolymer self-assembly and soft nanotransfer printing. *Polym. Chem.* **2019**, *10*, 3194−3200.
(21) Deubel, M.; von Freymann, G.; Wegener, M.; Pereira, S.; Busch, K.; Soukoulis, C. M. Direct laser writing of three-dimensional photonic-crystal templates for telecommunications. *Nat. Mater.* **2004**, *3*, 444−447.
(22) Rill, M. S.; Plet, C.; Thiel, M.; Staude, I.; von Freymann, G.; Linden, S.; Wegener, M. Photonic metamaterials by direct laser writing and silver chemical vapour deposition. *Nat. Mater.* **2008**, *7*, 543−546.
(23) Ye, J.; Tan, H.; Wu, S.; Ni, K.; Pan, F.; Liu, J.; Tao, Z.; Qu, Y.; Ji, H.; Simon, P.; Zhu, Y. Direct laser writing of graphene made from chemical vapor deposition for flexible, integratable micro-Supercapacitors with ultrahigh power output. *Adv. Mater.* **2018**, *30*, 1801384.
(24) Zhang, Z.; Wang, Y.; Wang, X. Nanoporous bimetallic Pt−Au alloy nanocomposites with superior catalytic activity towards electrooxidation of methanol and formic acid. *Nanoscale* **2011**, *3*, 1663−1674.
(25) Hayakawa, K.; Yoshimura, T.; Esumi, K. Preparation of gold−dendrimer nanocomposites by laser irradiation and their catalytic reduction of 4-nitrophenol. *Langmuir* **2003**, *19*, 5517−5521.
(26) Li, Y.; Ding, Y. Porous AgCl/Ag nanocomposites with enhanced visible light photocatalytic properties. *J. Phys. Chem. C* **2010**, *114*, 3175−3179.
(27) Sellinger, A. T.; Wang, D. H.; Tan, L.-S.; Vaia, R. A. Electrothermal polymer nanocomposite actuators. *Adv. Mater.* **2010**, *22*, 3430−3435.
(28) Yan, Y.; Santaniello, T.; Bettini, L. G.; Minnai, C.; Bellacicca, A.; Porotti, R.; Denti, I.; Faraone, G.; Merlini, M.; Lenardi, C.; Milani, P. Electroactive ionic soft actuators with monolithically integrated gold nanocomposite electrodes. *Adv. Mater.* **2017**, *29*, 1606109.
(29) Kumar, A.; Gullapalli, H.; Balakrishnan, K.; Botello-Mendez, A.; Vajtai, R.; Terrones, M.; Ajayan, P. M. Flexible ZnO−cellulose nanocomposite for multisource energy conversion. *Small* **2011**, *7*, 2173−2178.
(30) Lee, S.; Yeom, B.; Kim, Y.; Cho, J. Layer-by-layer assembly for ultrathin energy-harvesting films: Piezoelectric and triboelectric nanocomposite films. *Nano Energy* **2019**, *56*, 1−15.
(31) Arbab, E. A. A.; Mola, G. T. Metals decorated nanocomposite assisted charge transport in polymer solar cell. *Mater. Sci. Semicond. Process.* **2019**, *91*, 1−8.
(32) Jo, Y.; Cheon, J. Y.; Yu, J.; Jeong, H. Y.; Han, C.-H.; Jun, Y.; Joo, S. H. Highly interconnected ordered mesoporous carbon−carbon nanotube nanocomposites: Pt-free, highly efficient, and durable counter electrodes for dye-sensitized solar cells. *Chem. Commun.* **2012**, *48*, 8057−8059.
(33) Zhang, Z.; Zhang, L.; Hedhili, M. N.; Zhang, H.; Wang, P. Plasmonic gold nanocrystals coupled with photonic crystal seamlessly on TiO_2 nanotube photoelectrodes for efficient visible light photoelectrochemical water splitting. *Nano Lett.* **2013**, *13*, 14−20.
(34) Xiong, J.; Li, Z.; Chen, J.; Zhang, S.; Wang, L.; Dou, S. Facile synthesis of highly efficient One-dimensional plasmonic photocatalysts through Ag@Cu_2O core−shell heteronanowires. *ACS Appl. Mater. Interfaces* **2014**, *6*, 15716−15725.
(35) Imamura, S.; Tsuji, Y.; Miyake, Y.; Ito, T. Cooperative action of palladium and manganese(III) oxide in the oxidation of carbon monoxide. *J. Catal.* **1995**, *151*, 279−284.
(36) Zhang, H.; Hu, C.; Chen, S.; Zhang, K.; Wang, X. Synthesis of SnO_2 nanostructures and their application for hydrogen evolution reaction. *Catal. Lett.* **2012**, *142*, 809−815.
(37) Barman, S. C.; Hossain, M. F.; Yoon, H.; Park, J. Y. Trimetallic Pd@ Au@ Pt nanocomposites platform on-COOH terminated reduced graphene oxide for highly sensitive CEA and PSA biomarkers detection. *Biosens. Bioelectron.* **2018**, *100*, 16−22.
(38) Liu, J.; Lan, L.; Li, R.; Liu, X.; Wu, C. Agglomerated Ag−Pd catalyst with performance for hydrogen generation from formic acid at room temperature. *Int. J. Hydrogen Energy* **2016**, *41*, 951−958.
(39) Jiang, W.; Liu, H.; Yin, L.; Ding, Y. Fabrication of well-arrayed plasmonic mesoporous TiO_2/Ag films for dye-sensitized solar cells by multiple-step nanoimprint lithography. *J. Mater. Chem. A* **2013**, *1*, 6433−6440.
(40) Eom, H.; Jung, J.-Y.; Shin, Y.; Kim, S.; Choi, J.-H.; Lee, E.; Jeong, J.-H.; Park, I. Strong localized surface plasmon resonance effects of Ag/TiO_2 core−shell nanowire arrays in UV and visible light for photocatalytic activity. *Nanoscale* **2014**, *6*, 226−234.
(41) Zhao, Z.-J.; Lee, M.; Kang, H.; Hwang, S.; Jeon, S.; Park, N.; Park, S.-H.; Jeong, J.-H.; Park, S.-H.; Jeong, J. H. Eight inch wafer-scale flexible polarization-dependent color filters with Ag−TiO_2 composite nanowires. *ACS Appl. Mater. Interfaces* **2018**, *10*, 9188−9196.
(42) Zhao, Z.-J.; Hwang, S. H.; Jeon, S.; Hwang, B.; Jung, J.-Y.; Lee, J.; Park, S.-H.; Jeong, J.-H. Three-dimensional plasmonic Ag/TiO_2 nanocomposite architectures on flexible substrates for visible-light photocatalytic activity. *Sci. Rep.* **2017**, *7*, 8915.
(43) Zhao, Z.-J.; Gao, M.; Hwang, S.; Jeon, S.; Park, I.; Park, S.-H.; Jeong, J.-H. Heterogeneous nanostructures fabricated via binding energy-controlled nanowelding. *ACS Appl. Mater. Interfaces* **2019**, *11*, 7261−7271.
(44) Wronski, C. R. M. The size dependence of the melting point of small particles of tin. *Br. J. Appl. Phys.* **1967**, *18*, 1731−1737.
(45) Berman, R. P.; Curzon, A. E. The size dependence of the melting point of small particles of indium. *Can. J. Phys.* **1974**, *52*, 923−929.
(46) Zhao, Z.-J.; Hwang, S. H.; Jeon, S.; Jung, J.-Y.; Lee, J.; Choi, D.-G.; Choi, J.-H.; Park, S.-H.; Jeong, J.-H. Effects of polymer surface energy on morphology and properties of silver nanowire fabricated via

https://dx.doi.org/10.1021/acssensors.0c00211
ACS Sens. 2020, 5, 2367−2377

nanoimprint and E-beam evaporation. *Appl. Surf. Sci.* **2017**, *420*, 429−438.
(47) Hwang, S. H.; Zhao, Z.-J.; Jeon, S.; Kang, H.; Ahn, J.; Jeong, J. H. Repeatable and metal-independent nanotransfer printing based on metal oxidation for plasmonic color filters. *Nanoscale* **2019**, *11*, 11128−11137.
(48) Jiang, Q.; Zhang, S.; Zhao, M. Size-dependent melting point of noble metals. *Mater. Chem. Phys.* **2003**, *82*, 225−227.
(49) Zhao, Z.-J.; Shin, S.-H.; Choi, D.-G.; Park, S.-H.; Jeong, J.-H. Shape-controlled 3D periodic metal nanostructures fabricated via nanowelding. *Small* **2018**, *14*, 1703102.
(50) Ferhat-Hamida, Z.; Barbier, J., Jr.; Labruquere, S.; Duprez, D. The chemical state of palladium in alkene and acetylene oxidation: A study by XRD, electron microscopy and TD-DTG analysis. *Appl. Catal., B* **2001**, *29*, 195−205.
(51) Fan, J. C. C.; Bachner, F. J. Transparent heat mirrors for solar-energy applications. *Appl. Opt.* **1976**, *15*, 1012−1017.
(52) Gupta, R.; Rao, K. D. M.; Kiruthika, S.; Kulkarni, G. U. Visibly transparent heaters. *ACS Appl. Mater. Interfaces* **2016**, *8*, 12559−12575.
(53) Ingvarsson, S.; Klein, L.; Au, Y.-Y.; Lacey, J. A.; Hamann, H. F. Enhanced thermal emission from individual antenna-like nanoheaters. *Opt. Express* **2007**, *15*, 11249−11254.
(54) Dyatkin, B. Nano focus: Gold nanoheaters enable optically controlled soft robots. *MRS Bull.* **2018**, *43*, 647−648.
(55) Lu, X.; Zhang, Z.; Sun, X.; Chen, P.; Zhang, J.; Guo, H.; Shao, Z.; Peng, H. Flexible and stretchable chromatic fibers with high sensing reversibility. *Chem. Sci.* **2016**, *7*, 5113−5117.
(56) Kim, T.; Kim, Y. W.; Lee, H. S.; Kim, H.; Yang, W. S.; Suh, K. S. Uniformly interconnected silver-nanowire networks for transparent film heaters. *Adv. Funct. Mater.* **2013**, *23*, 1250−1255.
(57) Rathmell, A. R.; Wiley, B. J. The synthesis and coating of long, thin copper nanowires to make flexible, transparent conducting films on plastic substrates. *Adv. Mater.* **2011**, *23*, 4798−4803.
(58) Rathmell, A. R.; Bergin, S. M.; Hua, Y.-L.; Li, Z.-Y.; Wiley, B. J. The growth mechanism of copper nanowires and their properties in flexible, transparent conducting films. *Adv. Mater.* **2010**, *22*, 3558−3563.
(59) Jeong, H.; Choi, J.; Han, E. B.; Kuk, K.; Cheong, Y. M.; An, M. K. Image fusing apparatus using carbon nano-tube heater. U.S. Patent 8,995,894 B2, March 3, 2015.
(60) Cui, Z.; Han, Y.; Huang, Q.; Dong, J.; Zhu, Y. Electrohydrodynamic printing of silver nanowires for flexible and stretchable electronics. *Nanoscale* **2018**, *10*, 6806−6811.
(61) Arya, S. K.; Krishnan, S.; Silva, H.; Jean, S.; Bhansali, S. Advances in materials for room temperature hydrogen sensors. *Analyst* **2012**, *137*, 2743−2756.
(62) Sekimoto, S.; Nakagawa, H.; Okazaki, S.; Fukuda, K.; Asakura, S.; Shigemori, T.; Takahashi, S. A fiber-optic evanescent-wave hydrogen gas sensor using palladium-supported tungsten oxide. *Sens. Actuators, B* **2000**, *66*, 142−145.
(63) Choi, S.-J.; Chattopadhyay, S.; Kim, J. J.; Kim, S.-J.; Tuller, H. L.; Rutledge, G. C.; Kim, I.-D. Coaxial electrospinning of WO_3 nanotubes functionalized with Bio-inspired Pd catalysts and their superior hydrogen sensing performance. *Nanoscale* **2016**, *8*, 9159−9166.
(64) Favier, F.; Walter, E. C.; Zach, M. P.; Benter, T.; Penner, R. M. Hydrogen sensors and switches from electrodeposited palladium mesowire arrays. *Science* **2001**, *293*, 2227−2231.
(65) Chung, M. G.; Kim, D.-H.; Seo, D. K.; Kim, T.; Im, H. U.; Lee, H. M.; Yoo, J.-B.; Hong, S.-H.; Kang, T. J.; Kim, Y. H. Flexible hydrogen sensors using graphene with palladium nanoparticle decoration. *Sens. Actuators, B* **2012**, *169*, 387−392.
(66) Wang, M.; Feng, Y. Palladium−Silver Thin Film for Hydrogen Sensing. *Sens. Actuators, B* **2007**, *123*, 101−106.
(67) Jang, J.-S.; Qiao, S.; Choi, S.-J.; Jha, G.; Ogata, A. F.; Koo, W.-T.; Kim, D.-H.; Kim, I.-D.; Penner, R. M. Hollow Pd−Ag composite nanowires for fast responding and transparent hydrogen sensors. *ACS Appl. Mater. Interfaces* **2017**, *9*, 39464−39474.
(68) Li, X.; Liu, Y.; Hemminger, J. C.; Penner, R. M. Catalytically activated palladium@platinum nanowires for accelerated hydrogen gas detection. *ACS Nano* **2015**, *9*, 3215−3225.
(69) Namba, K.; Ogura, S.; Ohno, S.; Di, W.; Kato, K.; Wilde, M.; Pletikosić, I.; Pervan, P.; Milun, M.; Fukutani, K. Acceleration of hydrogen absorption by palladium through surface alloying with gold. *Proc. Natl. Acad. Sci. U.S.A.* **2018**, *115*, 7896−7900.
(70) Luna-Moreno, D.; Monzón-Hernández, D.; Villatoro, J.; Badenes, G. Optical fiber hydrogen sensor based on core diameter mismatch and annealed Pd−Au thin films. *Sens. Actuators, B* **2007**, *125*, 66−71.

https://dx.doi.org/10.1021/acssensors.0c00211
ACS Sens. 2020, 5, 2367−2377